# Crossed Andreev reflection in topological insulator nanowire T junctions

Jacob Fuchs,[1,*] Michael Barth,[1] Cosimo Gorini,[1,2] İnanç Adagideli,[3,4] and Klaus Richter[1]
[1]*Institut für Theoretische Physik, Universität Regensburg, 93040 Regensburg, Germany*
[2]*Université Paris-Saclay, CEA, CNRS, SPEC, 91191 Gif-sur-Yvette, France*
[3]*Faculty of Engineering and Natural Sciences, Sabancı University, 34956 Orhanlı-Tuzla, Turkey*
[4]*Faculty of Science and Technology and MESA+ Institute for Nanotechnology, University of Twente, 7500 AE Enschede, Netherlands*

(Received 16 April 2021; revised 15 July 2021; accepted 30 July 2021; published 12 August 2021)

We numerically study crossed Andreev reflection (CAR) in a topological insulator nanowire T junction where one lead is proximitized by a superconductor. We perform realistic simulations based on the three-dimensional (3D) Bernevig-Hughes-Zhang model and compare the results with those from an effective two-dimensional (2D) surface model, whose computational cost is much lower. Both approaches show that CAR should be clearly observable in a wide parameter range, including perfect CAR in a somewhat more restricted range. Furthermore, it can be controlled by a magnetic field and is robust to disorder. Our effective 2D implementation allows us to model systems of micron size, typical of experimental setups but computationally too heavy for 3D models.

DOI: 10.1103/PhysRevB.104.085415

## I. INTRODUCTION

The combination of superconductors with materials in the normal (N) conducting state led to the discovery of many interesting physical effects [1], a notable one being Andreev reflection (AR) [2]. In this process an incoming electron from the N contact is reflected as a hole by forming a Cooper pair in the superconductor. In the presence of a second N contact, the outgoing hole can leave either through the same normal lead as the incoming electron or through the other and spatially separated one. The second process is called crossed Andreev reflection (CAR) and amounts to the formation of a Cooper pair from two electrons from different leads. CAR is particularly interesting because of its nonlocal character. In fact, nonlocality can be exploited to generate entanglement via CAR's reciprocal process, i.e., the "splitting" of a Cooper pair into two entangled electrons leaving the system through different contacts. Cooper pair splitters, three-terminal setups with one superconducting and two normal contacts, have been investigated both theoretically (e.g., Refs. [3–5]) and experimentally (e.g., Refs. [6–8]). CAR has also been reported in experiments (e.g., Ref. [9]) and theoretical proposals, e.g., in the one-dimensional Kitaev chain [10] and many two-dimensional (2D) systems like graphene [11–13]. Moreover, this transport process was recently measured in the fractional quantum Hall edge [14]. However, CAR generally competes with normal electron transmission (T), where an electron is directly transferred from one normal lead to the other, bypassing the superconducting contact. Indeed, T usually dominates CAR. The dominating process can be identified with the nonlocal conductance, to which T and CAR contribute with opposite signs. It is always desirable to maximize the CAR rate in the system, in other words to achieve perfect CAR in the best case. Hence, there have been theoretical studies that considered systems where this process might be observable, like in bilayer graphene van der Waals hybrid structures [15], due to a Dirac semimetal in the quantum Hall regime [16] or by using 2D antiferromagnets [17]. They showed that perfect CAR can occur, but most of the time the effect strongly depends on geometrical properties or on the local doping level.

Topological insulators (TIs) exhibit a number of peculiar transport properties, e.g., surface or edge transport robust to disorder [18], helical edge modes in 2D TIs [19], topological superconductivity, and Majorana modes when proximitized by a superconductor [20,21]. CAR has been used to study topological phase transitions and Majorana zero modes [22–24] and was also reported in the presence of magnetic ordering [25,26] and in double TI Josephson junctions [27], couplings between the edges [28,29], odd-frequency triplet superconductivity [30,31], and when the system is arranged in a bipolar setup [32–34]. In this work, we propose an experimentally feasible setup allowing for detecting perfect CAR in a robust way over a large parameter range which can be controlled through an external magnetic field. To this end we propose a Cooper pair splitter setup based on a three-dimensional (3D) T-shaped TI junction, whose third lead is a normal-superconductor (NS) junction [see Fig. 1(a)]. In a simpler two-terminal geometry, i.e., a straight 3D TI nanowire, the NS contact allows for switching between (local) AR and electron reflection (R) by tuning a coaxial magnetic field [35]. Once embedded in our setup, the same NS contact allows for nonlocal switching between T and CAR by tuning $\vec{B}_{\parallel}$, which plays the role of the coaxial field of the two-terminal configuration. Furthermore, we will see that CAR is expected for a wide parameter range, suggesting the feasibility of our device with current technology.

This paper is straightforwardly organized: In Sec. II we describe the T-junction device and its working principles; Sec. III introduces the model and the numerical methods we base our simulations on, while Sec. IV discusses the numerical

*jacob.fuchs@physik.uni-regensburg.de

 

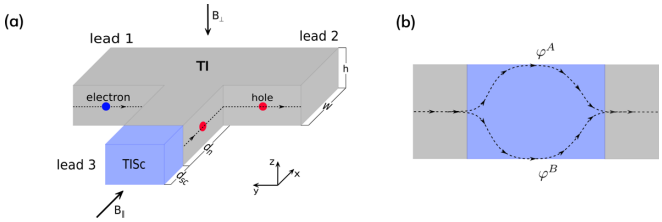


FIG. 1. (a) Schematic illustration of the suggested setup. The system consists of a junction of three TI nanowires in which one of them is proximitized by a normal $s$-wave superconductor. Furthermore, two magnetic field components are shown, a perpendicular one to induce chiral edge states and an axial magnetic field to tune the local AR at the interface. (b) Sketch illustrating the minimal model (presented at the end of Sec. II) based on two paths with phases $\varphi^A$ and $\varphi^B$ given in Eq. (1).

results. We conclude with a brief summary in Sec. V. Certain technicalities can be found in the Appendixes.

## II. T-JUNCTION DEVICE

### A. Previous work: NS junction

It is useful to start by recalling the main magnetotransport characteristics of the basic NS junction.

In 3D TI nanowires, an intrinsic Berry phase of $\pi$ leads to a gapped spectrum [18,36,37]. When a magnetic field $B_\parallel$ coaxial with the wire is switched on, the Berry phase competes with the resulting Aharonov-Bohm one, i.e., with the flux $\phi$ through the nanowire cross section. The latter tunes the spectrum and makes it gapless for $\phi = \phi_0/2$, with $\phi_0 = h/e$ being the flux quantum. At this half-integer value of $\phi$, topological superconductivity is induced in the system by proximity with a trivial superconductor [38,39], reverting back to triviality for other values of the flux. Topological and trivial regimes can be distinguished by the two-terminal conductance of a single NS junction [35]. The two regimes remain discernible when a strong perpendicular magnetic field $B_\perp$ is applied to the normal half of the system, provided it is screened on the superconducting side. Then, Landau levels and chiral edge states emerge [40–43]. In the single-mode regime, there is only one incoming channel on the one edge and one outgoing channel on the other edge. Incoming electrons are either perfectly reflected in the trivial regime (leading to a NS conductance of zero) or perfectly Andreev reflected in the topological regime (such that the NS conductance is $2e^2/h$). This effect arises from the flux $\phi = \phi_0/2$ threaded through the superconducting lead, introducing a vortex at the NS interface [39]. The vortex modifies Andreev reflection [35] by determining the matching angular momenta of electron and hole modes in the single-mode regime. In this regime a robust Andreev reflection signature can be obtained, which in turn can be used for a robust CAR process.

### B. Mechanics of the T junction

Incoming and outgoing quasiparticles are spatially separated, traveling along chiral edge states on opposite sides of the wire. To split them into separate leads, another nanowire is attached to get the T-shaped device shown in Fig. 1. In our case wires have a rectangular cross section, so that, strictly speaking, the edge states are actually side surface states. The magnetic field $B_\perp$ is perpendicular to the full T-junction structure, which is then, as a whole, in the quantum Hall regime, with Landau levels on the top and bottom T-shaped surfaces. The incoming and outgoing channels at the NS interface thus spatially separate, running into/coming from different normal leads. In this way, AR turns into CAR. The parallel magnetic field $B_\parallel$ now controls not only the AR at the NS interface but also the CAR of the entire device: For $\phi = 0$, we expect normal reflection at the NS interface and T in the entire device, while for $\phi = \phi_0/2$ we expect Andreev reflection and crossed Andreev reflection, respectively.

Note that $B_\parallel$ should not be strong enough to push the side T-junction surfaces into the quantum Hall regime. This condition is easily met in practice, as the height of typical nanowires is considerably smaller than their width (cf. Ref. [44], for example).

The essential physics can be captured with the single-particle Hamiltonian

$$H = -iv_F\partial_s + \tau_y(\partial_s\varphi^A - \partial_s\varphi^B)/4 + (\partial_s\varphi^A + \partial_s\varphi^B)/4, \quad (1)$$

which is similar to the Majorana interferometers from Refs. [23,24] (see also [22]). Here, $s$ is the coordinate along the chiral edge state; the two components with $\tau_y = \pm$ describe the paths of the two Majorana modes that make up the Dirac mode. In this basis the charge operator is diagonal and proportional to $\tau_z$. In our case these two possible paths go through the the upper and lower surfaces of the NS interface [see Fig. 1(b)]. $\varphi^{A/B}$ are the phases of the superconductor along the upper/lower path; $v_F$ is the Fermi velocity. It is then easy to see that the scattering matrix is given by

$$S(s) = \exp\left(\frac{i}{4}\tau_y\int^s[\partial_{s'}\varphi^A(s') - \partial_{s'}\varphi^B(s')]ds'\right) = (i\tau_y)^{N_v}, \quad (2)$$

where $N_v$ is the number of vortices enclosed between the two paths. We thus see that an odd number of vortices leads to perfect electron-hole conversion.

## III. METHODS

### A. Surface model

Due to the bulk being insulating, the system can be modeled by describing the surface states with a 2D Dirac Hamiltonian [18,36,43,44]. We use an approach similar to Ref. [43] which can be applied to arbitrarily shaped devices. The Hamiltonian of a surface with normal vector $\vec{n}$ reads

$$H_{\vec{n}} = \hbar v_F(\vec{\sigma}\times\vec{k})\cdot\vec{n} - \mu, \quad (3)$$

with $\vec{\sigma}$ being the vector of Pauli matrices and $\mu$ being the chemical potential. The wave functions of the different surfaces have to be matched at the edges, $\psi_1 = U\psi_2$, where $U$ is the appropriate spin rotation [45]. For the Fermi velocity, we use $\hbar v_F = 0.41$ eV nm for $Bi_2Se_3$ [46] and $\hbar v_F = 0.33$ eV nm for HgTe [44]. Superconductivity is modeled using the Bogoliubov–de Gennes formalism (see Sec. III C). The

magnetic field is described by the vector potential

$$\vec{A} = \vec{A}_{\parallel} + \vec{A}_{\perp} = \begin{pmatrix} 0 \\ -B_{\parallel} z/2 \\ B_{\parallel} y/2 \end{pmatrix} + \begin{pmatrix} 0 \\ -B_{\perp} x \\ 0 \end{pmatrix}. \tag{4}$$

The origin of the coordinate system is located at the NS interface in the center of the nanowire.

For the numerical simulations, we discretize the Hamiltonian to get a tight-binding model. To deal with fermion doubling [47–49], we add the quadratic term $[\vec{k}^2 - (\vec{k}\cdot\vec{n})^2]\,\vec{\sigma}\cdot\vec{n}$ to the Hamiltonian $H_{\vec{n}}$ in Eq. (3). The matching conditions $U$ between the surfaces also enter the edge hoppings, as can be seen in Appendix A. The magnetic field is introduced via Peierls substitution [50] (see Appendix B).

From the tight-binding model, we calculate the scattering matrix and transmission coefficients at zero energy using KWANT [51–53]. The conductances are given by [54]

$$\begin{aligned} G_{aa} &= \frac{\partial I_a}{\partial V_a}(V_a = 0) \\ &= \frac{e^2}{h}\left(N_a + T_{aa}^{\mathrm{AR}} - T_{aa}^{\mathrm{R}}\right), \end{aligned} \tag{5}$$

$$\begin{aligned} G_{ba} &= -\frac{\partial I_b}{\partial V_a}(V_a = 0) \\ &= \frac{e^2}{h}\left(T_{ba}^{\mathrm{T}} - T_{ba}^{\mathrm{CAR}}\right), \qquad a \neq b, \end{aligned} \tag{6}$$

where $I_b$ is the current from lead $b$ into the scattering region, $N_a$ is the number of modes in lead $a$, and $T_{aa}^{\mathrm{R}}$, $T_{aa}^{\mathrm{AR}}$, $T_{ba}^{\mathrm{T}}$, and $T_{ba}^{\mathrm{CAR}}$ are the transmission coefficients of the R (an electron from lead $a$ is reflected as an electron), the AR (an electron from lead $a$ is reflected as a hole), the T (an electron from lead $a$ is transmitted to lead $b$ as an electron), and the CAR (an electron from lead $a$ is transmitted to lead $b$ as a hole).

### B. Three-dimensional BHZ model

For our full 3D simulations we use the 3D BHZ Hamiltonian [46,55] in the basis $\{|p1_z^+\uparrow\rangle, |p2_z^-\uparrow\rangle, |p1_z^+\downarrow\rangle, |p2_z^-\downarrow\rangle\}$, that is,

$$\begin{aligned} H^{\mathrm{3D}} =& [\epsilon(\vec{k}) - \mu]\mathbb{1}_{4\times 4} \\ &+ \begin{pmatrix} M(\vec{k}) & A_1 k_z & 0 & A_2 k_- \\ A_1 k_z & -M(\vec{k}) & A_2 k_- & 0 \\ 0 & A_2 k_+ & M(\vec{k}) & -A_1 k_z \\ A_2 k_+ & 0 & -A_1 k_z & -M(\vec{k}) \end{pmatrix}. \end{aligned} \tag{7}$$

Here,

$$\epsilon(\vec{k}) = C + D_1 k_z^2 + D_2\left(k_x^2 + k_y^2\right), \tag{8}$$

$$M(\vec{k}) = M - B_1 k_z^2 - B_2\left(k_x^2 + k_y^2\right), \tag{9}$$

$$k_{\pm} = k_x \pm i k_y. \tag{10}$$

We use $Bi_2Se_3$ parameters (see Table I). Analogously to the 2D case, the Hamiltonian is discretized, turning it into a tight-binding form for implementation in KWANT. The cubic lattice has grid spacing $a = 1$ nm, and the magnetic fields enter as before via Peierls substitution [50].

TABLE I. Hamiltonian parameters for $Bi_2Se_3$.

| | |
|---|---|
| $M = 0.28$ eV | $A_1 = 2.2$ eV Å |
| $C = -0.0068$ eV | $A_2 = 4.1$ eV Å |
| $B_1 = 10$ eV Å$^2$ | $D_1 = 1.3$ eV Å$^2$ |
| $B_2 = 56.6$ eV Å$^2$ | $D_2 = 19.6$ eV Å$^2$ |

In the 3D model it is important for the axial magnetic field $B_{\parallel}$ to take into account the finite extension of the surface states into the bulk. This is of relevance, as we want to have a flux of $\phi = \phi_0/2$ penetrating the NS interface. The penetration depth of the surface states defines an effective cross-section area, and therefore, it is necessary to rescale the field strength [56]. In Appendix B the modified hoppings are given for the vector potential defined in Eq. (4). The orbital effect of the axial magnetic field is also considered inside the superconducting lead. The actual form of the vector potential becomes important in the case of superconducting systems, as it enters the gauge-invariant phase difference and determines the supercurrent density in the system [57]. In this work we adopt the choice of [58] and fixed the gauge to Eq. (4).

### C. Superconductivity

Superconductivity is modeled by the Bogoliubov–de Gennes Hamiltonian $H = \frac{1}{2}\Psi^{\dagger}\hat{H}\Psi$, with

$$\hat{H} = \begin{pmatrix} H & \Delta(\vec{r}) \\ \Delta^*(\vec{r}) & -\mathbb{T}^{-1} H \mathbb{T} \end{pmatrix}, \tag{11}$$

where $H$ is either the effective 2D Hamiltonian from Eq. (3) or the full 3D Hamiltonian from Eq. (7). The parameter $\Delta$ is the superconducting pairing potential, which depends on the spatial coordinate $\vec{r}$ and a complex phase $\chi$. The pairing potential is defined as

$$\Delta(\vec{r}) = \Delta(r)\exp[i\chi(y,z)], \tag{12}$$

where

$$\Delta(r) = \begin{cases} \Delta_0, & x < d_{sc}, \\ 0, & x > d_{sc}, \end{cases} \tag{13}$$

with $\Delta_0 = 0.25$ meV [35]. The Hamiltonian (11) is then discretized and implemented in tight-binding form with vanishing pairing potential in the normal regions.

Due to the fact that we are also considering the orbital effect of the axial magnetic field in the superconducting contact, the phase of the pairing potential will depend on the applied field strength and the spatial coordinates. Recall that a flux $\phi = \phi_0/2$ penetrating the superconducting wire cross section is expected to introduce a vortex at the NS interface. The vortex in our system is defined as

$$\chi(y,z) = \left\lfloor 2\frac{\phi}{\phi_0} \right\rfloor \begin{cases} \arctan\left(\frac{z}{y}\right), & \arctan\left(\frac{z}{y}\right) > 0, \\ 2\pi + \arctan\left(\frac{z}{y}\right), & \arctan\left(\frac{z}{y}\right) < 0, \end{cases}$$

with $\lfloor x \rfloor$ being the floor function. For simplicity, as we consider only surface states, we neglect the decrease of the pairing potential amplitude into the bulk due to the vortex. Moreover, in Appendix D we show that CAR is also modified by a vortex

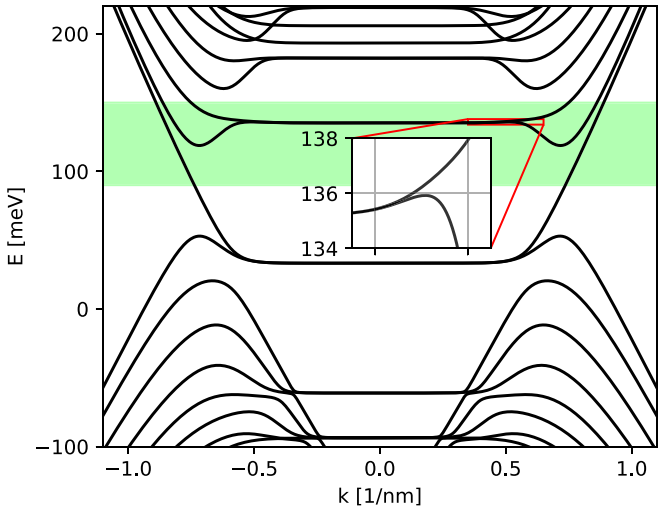


FIG. 2. Band structure of a TI nanowire of width $w = 50$ nm and height $h = 10$ nm in a perpendicular magnetic field $B_\perp = 20$ T calculated for the 3D BHZ model. The asymmetry with respect to the zeroth Landau level stems from the anisotropy in the $Bi_2Se_3$ crystal structure. The green shaded region corresponds to the energy range for our numerical transport calculations. This energy range corresponds to a peak in the transmission coefficients shown in Fig. 3. Inset: Zoom of the edge of the first Landau level.

that is, for example, pinned to a magnetic impurity. Note that in that case the superconducting pair potential $\Delta$ needs to be strong enough that the winding in the phase does not result in a closing of the superconducting band gap.

## IV. RESULTS

### A. Occurrence of CAR

First, we simulate a $Bi_2Se_3$ T junction with wires of width $w = 50$ nm and height $h = 10$ nm; $d_{sc} = 1$ nm, and $d_n = 20$ nm (see Fig. 1). These or larger dimensions are experimentally realizable [59]. We use $B_\perp = 20$ T such that the wires are in the quantum Hall regime (see Fig. 2). Wires with larger diameters allow for smaller magnetic fields $B_\perp$ (see below) but are computationally more demanding. Nevertheless, the transport signatures should not change qualitatively for larger systems.

The sign of $B_\perp$ is chosen such that modes incoming from the left lead hit the NS interface, whereas those from the right lead stay on the back side of the device and thus never reach the NS junction. Since we focus on CAR, we restrict ourselves to incoming electrons from the left lead.

Without axial magnetic field ($B_\parallel = 0$), there is perfect electron transmission and no CAR for $\mu < 118$ meV, as can be seen in Fig. 3(a). At $\mu \approx 118$ meV, an additional counterpropagating mode appears [42], coming from the small side minima of the Landau levels seen in Fig. 2. Therefore, reflection processes (R and AR) become possible. At $\mu \approx 135$ meV, the first Landau level is crossed. The transmission peak and higher number of overall modes at $\mu \approx 135$ meV are due to the Landau levels not being perfectly flat. The 3D model anisotropy causes a small distortion of the Landau level dispersion in the $k$ region just before the strong side upward bending: The dispersion is slightly S shaped (see the inset in Fig. 2), resulting in a small energy range with five modes rather than three. This signature is absent in the 2D model, as the latter is isotropic. For larger values of $\mu$, only T and CAR are possible.

Next, we use an axial magnetic field of $B_\parallel = 4.6$ T to induce a flux $\phi \approx \phi_0/2$ through the NS interface, inducing a vortex (see Sec. III C). The transmission coefficients are shown in Fig. 3(c). The single-mode regime now exhibits perfect CAR in the energy range $\mu < 118$ meV. Reflection processes appear as before only for $118 < \mu < 135$ meV due to counterpropagating modes. CAR persists at higher energies, but T becomes dominant in that range. The switching of T and CAR around $\mu \approx 138$ meV is a numerical issue. It appears because of an artificial mode mismatch at the NS interface between the superconducting lead, which hosts a vortex when $\phi = \phi_0/2$, and the nanowire surface states. The flux enclosed by the latter is not exactly $\phi_0/2$, as the states extend a few sites into the 3D bulk. The closer the value approaches the nominal $\phi_0/2$ in the superconducting lead, the smaller the numerical glitch is. Figure 4 shows the nonlocal conductances for the same system. For $\phi \approx \phi_0/2$, the conductance is quantized and negative, meaning that a voltage bias at the left lead drives a current into the device and out to the right lead. Note that the sign of the conductance indicates the direction of current flow in the right lead and therefore whether CAR or T dominates. The edge states for higher energies allow the conductance to become positive again, meaning that the current in the right lead is directed out of the device. For the applied perpendicular magnetic field strength it is more likely for those states to experience normal reflection at the NS interface. Therefore, the relative importance of CAR in the conductance drops.

The surface model results [Figs. 3(b) and 3(d)] are in good agreement with those from the 3D BHZ model. Note that there is a shift in the energy domain since the surface model does not account for the offset of the BHZ Hamiltonian.

Similar results are obtained for HgTe nanowires (see Fig. 5). The simulations are performed for wires of width $w = 160$ nm and height $h = 70$ nm, corresponding to the recent experimental sample sizes [44]. In this system a perpendicular field $B_\perp = 1$ T is enough to drive the system into the quantum Hall regime since the corresponding magnetic length $l_B = \sqrt{\hbar/eB_\perp} \approx 26\,\text{nm} \ll w$.

As a last remark in this section, we discuss the case of axial magnetic fields differing from the special values we considered so far. In principle, we are just applying the external magnetic field in order to stabilize the vortex at the interface and to produce a robust superconducting state where all subbands are gapped. This field is not necessary because the vortex can also emerge from other sources and the presence of this winding is enough to observe the above-mentioned conductance signatures (see Appendix D). The winding of the phase can appear in a certain field range around half of a magnetic flux quantum; therefore, an exact fine tuning of the magnetic field is not necessary. In that field range the main conductance features persist. Only for larger field deviations from $\phi = \phi_0/2$ and in the case that no winding of the phase can emerge will superconductivity be destroyed by the

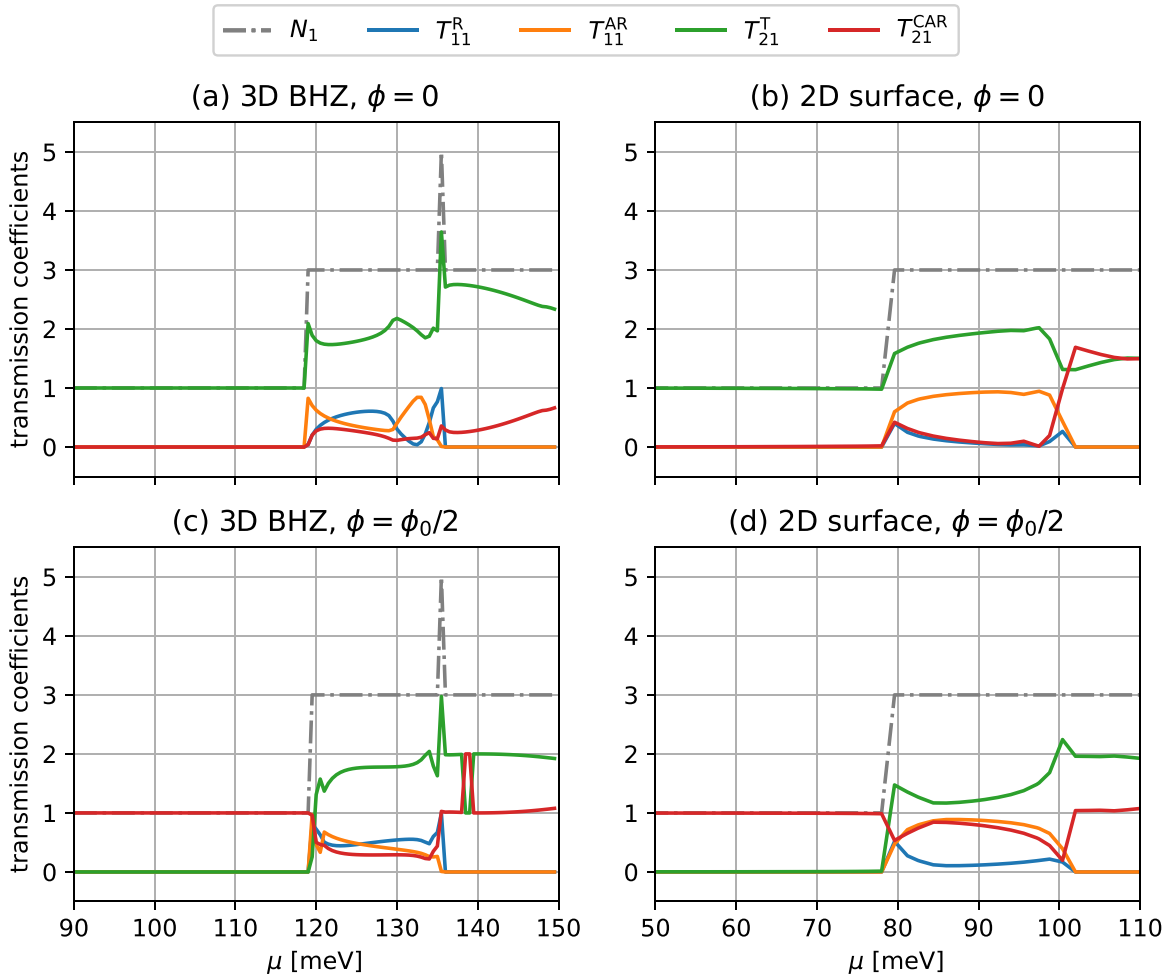


FIG. 3. Transmission coefficients of the T-junction device from Fig. 1. (a) and (c) show results obtained from the 3D BHZ model (Sec. III B) for $Bi_2Se_3$, and (b) and (d) represent results from the 2D surface model (Sec. III A). The height and width of the nanowires are $h = 10$ nm and $w = 50$ nm, and the magnetic field is $B_\perp = 20$ T.

external magnetic field as the gap starts to decrease. After the superconducting gap is closed, mainly transport from lead 1 into lead 3 will be present, as the chiral edge states can then enter into lead 3. When superconductivity is eventually lost depends strongly on the diameter and the symmetry properties of the nanowires [58].

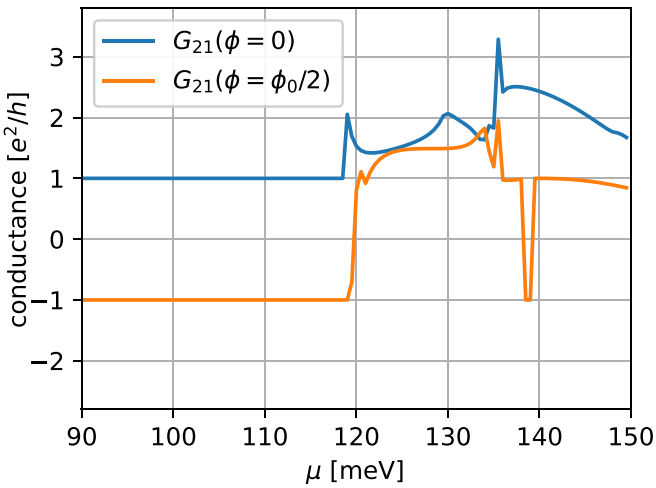


FIG. 4. Nonlocal conductance of the T-junction device from Fig. 1 obtained from the 3D BHZ model [see Eq. (7)] for $Bi_2Se_3$ [see Fig. 3(a) and 3(c)]. Negative conductance indicates CAR.

### B. Weak perpendicular magnetic field

Experimentally, it can be quite challenging to tune the system close to the Dirac point and to access the single-mode regime. For a clear and robust CAR signature it is desirable to operate the device in this energy range. The requirement is, however, not necessary, as CAR signatures can be obtained also in other parameter regimes.

We show the occurence of CAR on other parameter regimes by calculating a 2D density plot of the nonlocal conductance as a function of the chemical potential $\mu$ and of the perpendicular magnetic field $B_\perp$. In Fig. 6 blue regions correspond to a negative conductance $G_{21}$, a clear signature that CAR dominates over normal electron transmission. For this calculation the T-junction size was reduced to decrease computational costs. Below we will revert to the larger system of Sec. IV A and show that the obtained results also apply

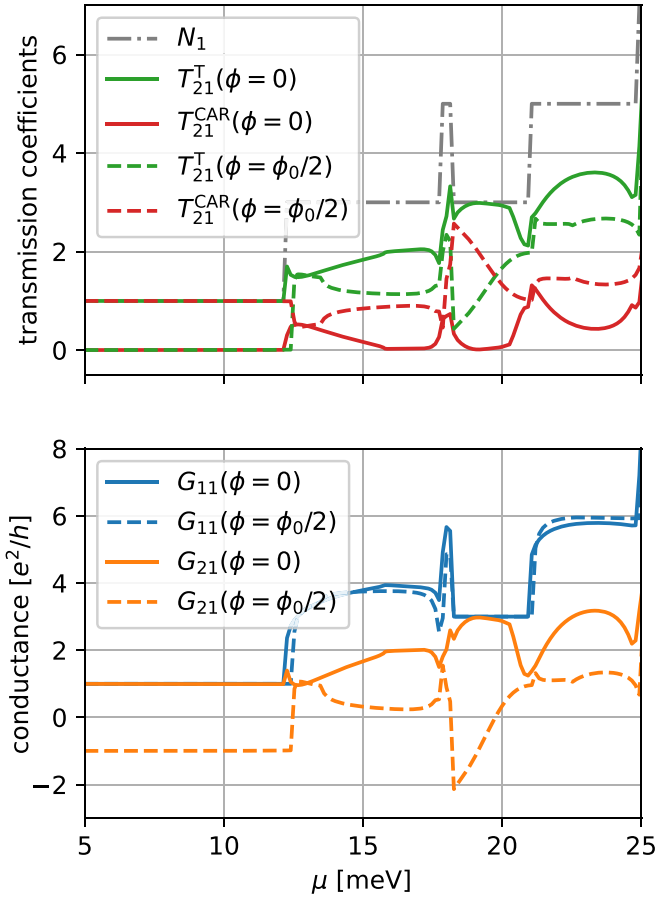


FIG. 5. Transmission coefficients and conductances of the T-junction device (see Fig. 1) calculated with the surface model from Sec. III A. The parameters are chosen to match the experimental values for HgTe nanowires from Ref. [44]: $h = 70\,\text{nm}$, $w = 160\,\text{nm}$, and $B_\perp = 1\,\text{T}$; a vortex in the superconducting contact is present for $\phi = \phi_0/2$.

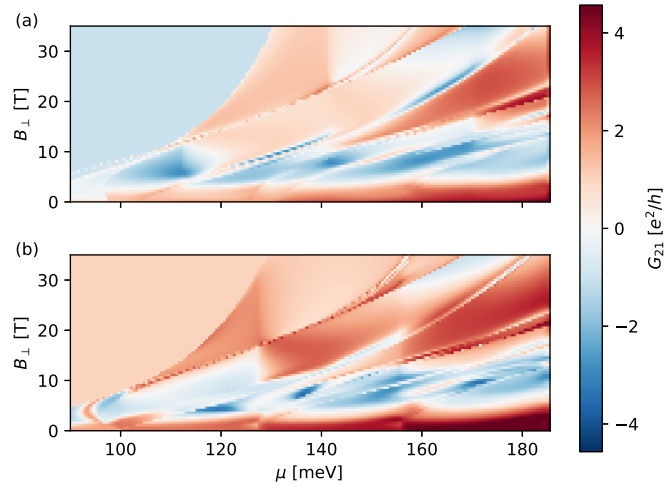


FIG. 6. Nonlocal conductance $G_{21}$ of a T-junction device with a nanowire width of $w = 24\,\text{nm}$ and a height of $h = 10\,\text{nm}$ as a function of the applied perpendicular magnetic field $B_\perp$ and the chemical potential $\mu$. In (a) a vortex is introduced at the NS interface by an axial magnetic field of $B_\parallel = 9.58\,\text{T}$, while in (b) no axial field or vortex is present. Positive conductance (red) indicates that the usual electron transmission dominates CAR ($T_{21}^{T} > T_{21}^{CAR}$), whereas negative conductance (blue) indicates dominating CAR ($T_{21}^{CAR} > T_{21}^{T}$).

for wider nanowires. The nanowire width and height are, respectively, $w = 24\,\text{nm}$ and $h = 10\,\text{nm}$. The parallel magnetic field was adjusted to give almost exactly a flux $\phi = \phi_0/2$ through the NS interface with $B_\parallel = 9.58\,\text{T}$ in Fig. 6(a), while in Fig. 6(b) no axial magnetic field was used. The field component parallel to the superconducting lead clearly enhances the CAR signature in a broad parameter range. Nevertheless, even without a vortex at the NS interface, a CAR signature is present in the lower field range over a wide $\mu$ interval. For larger systems similar behavior will take place at lower scales of $B_\perp$ and $\mu$.

Having established that CAR dominates in a fairly large parameter range, let us switch back to a larger system with a wire width of $w = 50\,\text{nm}$. As opposed to Sec. IV A, where $B_\perp = 20\,\text{T}$, we now perform a second calculation at a lower field strength of $B_\perp = 4\,\text{T}$. Figure 7(a) shows the band structure for this parameter set, with the green shaded region marking the energy range used in transport calculations. Flat Landau levels and the corresponding chiral edge states start to form. The transmission coefficients for zero axial field ($\phi = 0$) and $B_\parallel = 4.6\,\text{T}$ ($\phi = \phi_0/2$) are illustrated in Figs. 7(b) and 7(d), respectively. In the single-mode regime switching between no CAR and a robust CAR plateau takes place. However, contrary to the strong-field case in Fig. 3, a strong CAR signature survives at higher energies. It is also clearly observable in Fig. 7(c), where the nonlocal conductance is depicted.

Finally, we want to point out that the obtained results are also valid in a large parameter set when the Zeeman effect is also taken into account. A detailed discussion of this effect can be found in Appendix C.

### C. Disordered systems

We test the resilience of CAR signatures to impurities and imperfections, typically present in experimental setups, by performing simulations in disordered samples. We use short-range (white noise) disorder [60]. The on-site disorder is chosen from standard normal distribution with amplitude $U = K_0 \times 0.41\,\text{eV}$. Figure 8 shows a comparison of the simulation results between the clean and disordered cases. In order to get rid of at least the most significant disorder configuration dependent effects we averaged over 20 disorder sets. For the nanowire dimension we chose the same parameters as we used in Fig. 6 and set the perpendicular field to $B_\perp = 7\,\text{T}$. These settings allow us to determine whether the conductance shown in that density plot is robust to the applied disorder. The length parameters were $d_n = 20\,\text{nm}$ and $d_{sc} = 5\,\text{nm}$, so that the NS interface lies inside the disordered region. Also we put a distance of 45 nm between normal leads 1 and 2, so that the incoming modes can possibly scatter already before the NS interface.

By comparing the results of the clean and disordered simulations one clearly sees that the CAR plateau in the single-mode regime is still present. At larger energies the disorder reduces the CAR rate, but it is still present there. The disorder introduces scattering between chiral edge states of

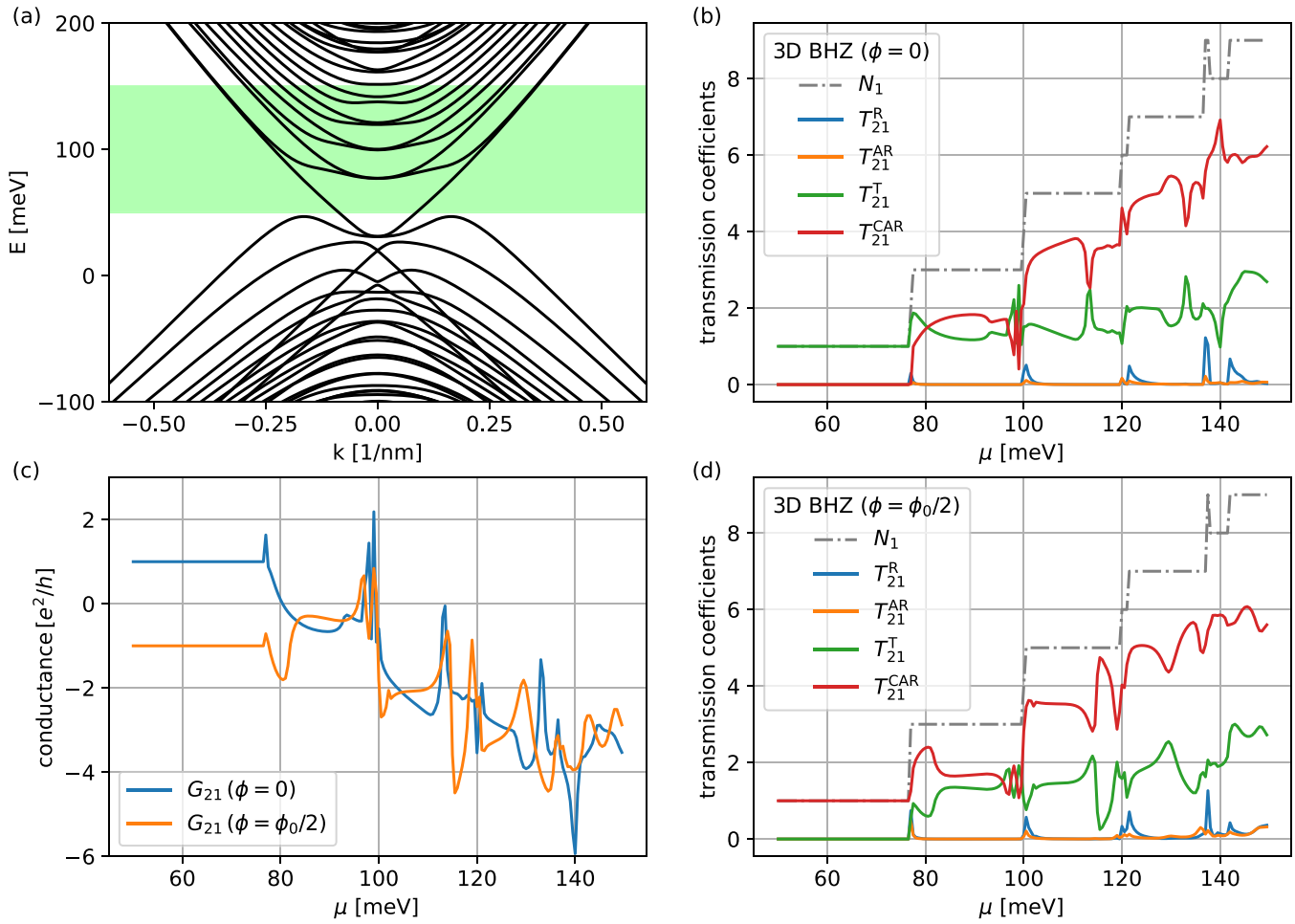


FIG. 7. (a) Band structure of a TI nanowire with a width of $w = 50$ nm and a height of $h = 10$ nm in a perpendicular magnetic field of $B_\perp = 4$ T calculated for the 3D BHZ model. The green shaded region corresponds again to the energy range for our numerical transport calculations. In (b) and (d) the transmission coefficients for $B_\parallel = 0$ and $B_\parallel = 4.6$ T are shown. (c) Nonlocal conductance calculated with Eq. (6).

the two side surfaces; therefore, backscattering and normal electron to electron transmission are enhanced. This effect should be reduced in nanowires with a larger width, which further separates the side surfaces. We conclude that in real devices the CAR signature should survive a certain amount of impurities and defects.

## V. CONCLUSION

We proposed a device that could be operated as a Cooper pair splitter based on a 3D TI T junction with one arm in proximity to an *s*-wave superconductor. The device working principle was studied by examining the inverted process, namely, crossed Andreev reflection, which is tunable by external magnetic fields of moderate magnitude. Numerical simulations for experimentally relevant parameter ranges (system size, magnetic field strength, disorder) show clear CAR signatures in the transmission coefficients and the nonlocal conductance. Signatures can be switched on and off and are more robust in the single-mode regime, which requires stronger fields ($\gtrsim$1 T) and a relatively fine tuning of the electrochemical potential near the Dirac point. However, they are present and fairly disorder resistant in a wider parameter range. The Cooper pair splitter, in turn, should then reliably act as a generator of entangled electron pairs.

On the theory side, we also implemented a 2D effective surface model which is computationally much lighter than a full 3D simulation yet produces qualitatively identical transport results. The 2D model allows treatment of micron-size 3D TI devices, currently computationally too demanding for full 3D simulations.

## ACKNOWLEDGMENTS

This work was supported by Deutsche Forschungsgemeinschaft (DFG, German Research Foundation) within Project No. 314695032-SFB 1277 (Project No. A07) and the Elitenetzwerk Bayern Doktorandenkolleg "Topological Insulators." We thank R. Kozlovsky for useful conversations.

## APPENDIX A: MATCHING CONDITION

In constructing the tight-binding Hamiltonian, we use the finite differences

$$\partial_x \psi(x_i) \approx \frac{-i}{2a}[\psi(x_{i+1}) - \psi(x_{i-1})]. \tag{A1}$$

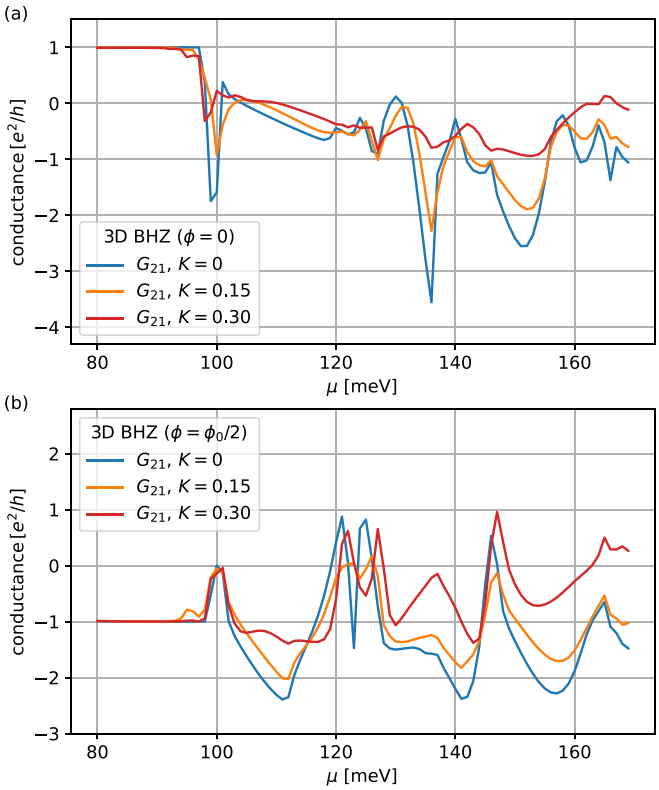


FIG. 8. Comparison between the conductance of a clean T junction and a disordered setup for an axial flux of (a) $\phi = 0$ and (b) $= \phi = \phi_0/2$. The disorder conductance was averaged over 20 configurations. The plateau in the single-mode regime is robust to the applied disorder.

Thus, the term $\hbar v_F k_x \sigma_y$ in the Hamiltonian yields the hoppings $t_{i,i+1} = -i\hbar v_F \sigma_y/2a$ from $x_i$ to $x_{i+1}$ and $t_{i+1,i} = i\hbar v_F \sigma_y/2a$ ($a$ is the grid spacing $x_{i+1} - x_i$). At the edge, one has $\psi_1 = U\psi_2$, so that, say,

$$\psi_2(x_{i+1}) = U^\dagger \psi_1(x_{i+1}) \tag{A2}$$

and

$$\partial_x \psi_1(x_i) \approx \frac{-i}{2a}[U^\dagger \psi_2(x_{i+1}) - \psi_1(x_{i-1})]. \tag{A3}$$

Then, the edge hoppings read $t_{i,i+1} = -i\hbar v_F \sigma_y U/2a$ and $t_{i+1,i} = i\hbar v_F U^\dagger \sigma_y/2a$.

As an example, consider the edge between the $\check{z}$ and $\check{x}$ surfaces. Then, $\psi_{\check{z}} = U\psi_{\check{x}}$ on the edge where $U = \exp(-i\pi\sigma_y/4) = (1 - i\sigma_y)/\sqrt{2}$ is the spin rotation around the $\check{y}$ axis by $\pi/2$. Indeed, one finds

$$U H_{\check{z}}(k_x = k_{-z}, k_y = k_y) U^\dagger = H_{\check{x}}. \tag{A4}$$

On the $\check{z}$ surface, the finite-difference method yields the hoppings $t_{i,i+1} = -i\hbar v_F \sigma_y/2a$ and $t_{i+1,i} = i\hbar v_F \sigma_y/2a$ in the $\check{x}$ direction. At the edge $(x, y, z) = (x_e, y_e, z_e)$, one has

$$\psi_i = \psi_{\check{z}}(x_e - a, y_e, z_e), \tag{A5}$$

$$\psi_{i+1} = \psi_{\check{x}}(x_e, y_e, z_e) = U^\dagger \psi_{\check{z}}(x_e, y_e, z_e), \tag{A6}$$

such that $t_{i,i+1} = -i\hbar v_F \sigma_z U/2a$ and $t_{i+1,i} = t^\dagger_{i,i+1} = i\hbar v_F U^\dagger \sigma_z/2a$.

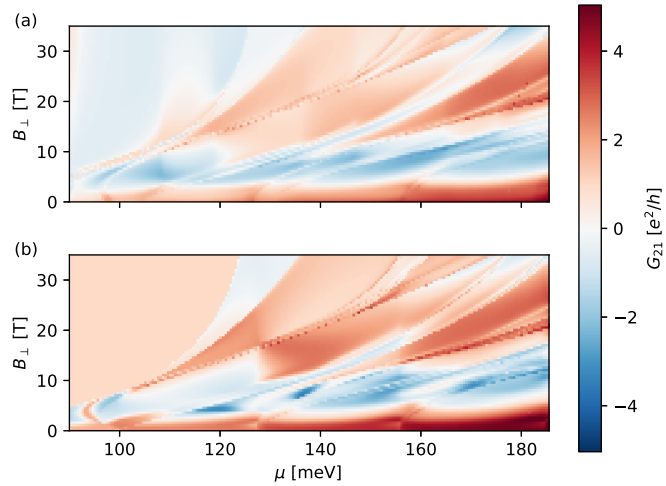


FIG. 9. Nonlocal conductance $G_{21}$ of the same system which was used for Fig. 6 depending on the applied perpendicular magnetic field $B_\perp$ and the chemical potential $\mu$. In (a) a vortex is again introduced at the NS interface by an axial magnetic field of $B_\parallel = 9.58$ T, while in (b) no axial field or vortex is applied. Again, positive conductance (red) indicates dominating electron transmission ($T_{21}^{\mathrm{T}} > T_{21}^{\mathrm{CAR}}$), and negative conductance (blue) indicates dominating CAR ($T_{21}^{\mathrm{CAR}} > T_{21}^{\mathrm{T}}$).

## APPENDIX B: PEIERLS'S SUBSTITUTION

For the setup to work efficiently we need magnetic field components. These can be included in the numerical implementation via Peierls's substitution [50]

$$t_{x/y/z} = t_{x/y/z}(B = 0) \exp\left(-i\frac{e}{\hbar}\int \vec{A}\cdot\vec{dl}\right). \tag{B1}$$

The hopping terms are then modified according to

$$t_y = t_y(\vec{B} = 0) \exp\left(i\frac{2\pi}{\phi_0}\frac{B_\parallel}{2c}a_z + i\frac{2\pi}{\phi_0}B_\perp a_x\right),$$

$$t_z = t_z(\vec{B} = 0) \exp\left(-i\frac{2\pi}{\phi_0}\frac{B_\parallel}{2c}a_y\right),$$

$$c \approx 1 - \frac{\langle\lambda\rangle C}{2A_{cs}}$$

where $C$ is the circumference of the nanowire and $A_{cs}$ is the nanowire cross section. The factor of $c$ is necessary to rescale the flux, as in the 3D model the surface states have a finite extension into the bulk [56]. The parameter $\langle\lambda\rangle$ is the mean penetration depth of the surface states. In small nanowires the penetration into the bulk will lead to an effective cross section area which is smaller than the actual wire cross section. For the surface model, $c = 1$.

## APPENDIX C: INFLUENCE OF THE ZEEMAN EFFECT

In the main text we considered the orbital effects of the applied magnetic fields. Here, we show that the obtained results should also be observable in systems with a Zeeman term due to large $g$ factors. As an example we are computing again the conductance map shown in Fig. 6 for $Bi_2Se_3$ with

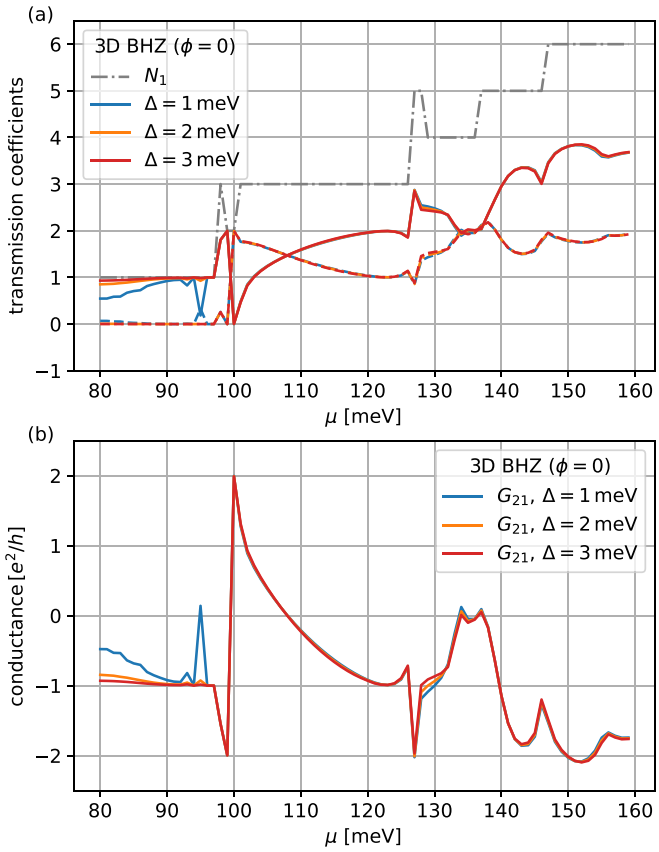


FIG. 10. Results for a transport calculation in the T-junction setup without an axial magnetic field, but in the presence of a vortex at the NS interface that might be present due to a magnetic impurity. In (a) the transmission coefficients for $T_{21}^{\mathrm{CAR}}$ and $T_{21}^{\mathrm{T}}$ are shown by solid and dashed lines, respectively. (b) plots the corresponding conductance.

the additional Zeeman Hamiltonian [61]

$$H_Z = \frac{\mu_B}{2}\begin{pmatrix} g_z^v B_z & 0 & g_P^v B_- & 0 \\ 0 & g_z^c B_z & 0 & -g_P^c B_- \\ g_P^v B_+ & 0 & -g_z^v B_z & 0 \\ 0 & g_P^c B_+ & 0 & -g_z^c B_z \end{pmatrix},$$

where $g_z^{v/c}$ and $g_P^{v/c}$ are the conduction ($c$) and valence ($v$) band $g$ factors of magnetic fields applied parallel and perpendicular to the $z$ axis, respectively, and $B_\pm = B_x \pm iB_y$. For the $g$ factors of $Bi_2Se_3$ we put [62] $g_z^v = 29.90$, $g_z^c = 27.3$, $g_P^v = 18.96$, and $g_P^c = 19.48$.

We are again differentiating between an applied axial magnetic field [Fig. 9(a)] and no field [Fig. 9(b)]. The Zeeman effect is taken into account in the whole system where also an orbital effect is present, meaning that in the superconducting part only the axial component is needed. The calculated conductance values are shown in Fig. 9. In the case of no axial magnetic field the computed conductance looks very similar to the result of the no Zeeman effect term with only some small changes in the high-field range. Switching on this field, the effect of this component turns out to be more important, as it is also present in the superconducting region. It leads to a small decrease in the overall CAR magnitude as well as to the opening of positive conductance regions in the single mode regime.

Note that we are considering a relatively small system geometry due to the numerical efforts for the 3D model. Therefore and due to the large $g$-factors of $Bi_2Se_3$, the emerging Zeeman terms are already very large and would be accordingly smaller in bigger realistic setups. Nevertheless, even for the large $B$ field values used here, the main features are still present, namely a broad parameter range for perfect CAR in the single-mode regime and a high CAR rate in the low-field regime.

## APPENDIX D: CAR WITH VORTEX AND NO AXIAL MAGNETIC FIELD

So far we have focused on the case of a vortex in the NS interface stabilized by an external axial magnetic field. Such a vortex could also be present, in metastable form, in the absence of a magnetic field if it is pinned to an impurity at the interface. As a final check, we also considered such a possibility in our numerical simulations. For the system configuration that was also used in Fig. 6 the results are presented in Fig. 10. A winding in the phase of $\Delta$ will disturb the superconducting pairing and diminish the superconducting gap in the band structure. This can be understood by performing a unitary gauge transformation that will get rid of the phase winding in $\Delta$ and simultaneously introduce an effective magnetic field along the wire direction, in addition to the statistical gauge field. Therefore, the situation is analogous to the case studied in [58], where the authors showed that an axial magnetic field will reduce the superconducting band gap. This is also visible in our setup, especially in the low-energy range. Thus, in order to reduce the transmission into the superconducting lead, one needs to increase the magnitude $\Delta$, so that the pairing survives the influence of the phase winding in the nanowire. In agreement with the theoretical expectations, we recover the perfect CAR in this limit.

[1] M. Tinkham, *Introduction to Superconductivity*, 2nd ed. (McGraw-Hill, New York, 1996).

[2] A. F. Andreev, The thermal conductivity of the intermediate state in superconductors, Zh. Eksp. Teor. Fiz. **46**, 1823 (1964); **49**, 655 (1965) [Sov. Phys. JETP **19**, 1228 (1964); **22**, 455 (1966)].

[3] G. Deutscher and D. Feinberg, Coupling superconducting-ferromagnetic point contacts by Andreev reflections, Appl. Phys. Lett. **76**, 487 (2000).

[4] G. B. Lesovik, T. Martin, and G. Blatter, Electronic entanglement in the vicinity of a superconductor, Eur. Phys. J. B **24**, 287 (2001).

[5] P. Recher, E. V. Sukhorukov, and D. Loss, Andreev tunneling, Coulomb blockade, and resonant transport of nonlocal spin-entangled electrons, Phys. Rev. B **63**, 165314 (2001).

[6] L. Hofstetter, S. Csonka, J. Nygård, and C. Schönenberger, Cooper pair splitter realized in a two-quantum-dot Y-junction, Nature (London) **461**, 960 (2009).

[7] L. G. Herrmann, F. Portier, P. Roche, A. L. Yeyati, T. Kontos, and C. Strunk, Carbon Nanotubes as Cooper-Pair Beam Splitters, Phys. Rev. Lett. **104**, 026801 (2010).

[8] J. Schindele, A. Baumgartner, and C. Schönenberger, Near-Unity Cooper Pair Splitting Efficiency, Phys. Rev. Lett. **109**, 157002 (2012).

[9] D. Beckmann, H. B. Weber, and H. v. Löhneysen, Evidence for Crossed Andreev Reflection in Superconductor-Ferromagnet Hybrid Structures, Phys. Rev. Lett. **93**, 197003 (2004).

[10] R. Nehra, D. S. Bhakuni, A. Sharma, and A. Soori, Enhancement of crossed Andreev reflection in a Kitaev ladder connected to normal metal leads, J. Phys.: Condens. Matter **31**, 345304 (2019).

[11] H. Haugen, D. Huertas-Hernando, A. Brataas, and X. Waintal, Crossed Andreev reflection versus electron transfer in three-terminal graphene devices, Phys. Rev. B **81**, 174523 (2010).

[12] R. Beiranvand, H. Hamzehpour, and M. Alidoust, Nonlocal Andreev entanglements and triplet correlations in graphene with spin-orbit coupling, Phys. Rev. B **96**, 161403 (2017).

[13] M. Beconcini, M. Polini, and F. Taddei, Nonlocal superconducting correlations in graphene in the quantum Hall regime, Phys. Rev. B **97**, 201403(R) (2018).

[14] Gül, Y. Ronen, S. Y. Lee, H. Shapourian, J. Zauberman, Y. H. Lee, K. Watanabe, T. Taniguchi, A. Vishwanath, A. Yacoby, and P. Kim, Induced superconductivity in the fractional quantum Hall edge, arXiv:2009.07836.

[15] X. Wu, H. Meng, F. Kong, H. Zhang, Y. Bai, and N. Xu, Tunable nonlocal valley-entangled Cooper pair splitter realized in bilayer-graphene van der Waals spin valves, Phys. Rev. B **101**, 125406 (2020).

[16] S.-B. Zhang and B. Trauzettel, Perfect Crossed Andreev Reflection in Dirac Hybrid Junctions in the Quantum Hall Regime, Phys. Rev. Lett. **122**, 257701 (2019).

[17] M. F. Jakobsen, A. Brataas, and A. Qaiumzadeh, Electrically Controlled Crossed Andreev Reflection in Two-Dimensional Antiferromagnets, Phys. Rev. Lett. **127**, 017701 (2021).

[18] J. H. Bardarson, P. W. Brouwer, and J. E. Moore, Aharonov-Bohm Oscillations in Disordered Topological Insulator Nanowires, Phys. Rev. Lett. **105**, 156803 (2010).

[19] G. Tkachov and E. M. Hankiewicz, Spin-helical transport in normal and superconducting topological insulators, Phys. Status Solidi B **250**, 215 (2013).

[20] M. Z. Hasan and C. L. Kane, *Colloquium*: Topological insulators, Rev. Mod. Phys. **82**, 3045 (2010).

[21] Y. Tanaka, M. Sato, and N. Nagaosa, Symmetry and topology in superconductors—Odd-frequency pairing and edge states, J. Phys. Soc. Jpn. **81**, 011013 (2012).

[22] J. Nilsson, A. R. Akhmerov, and C. W. J. Beenakker, Splitting of a Cooper Pair by a Pair of Majorana Bound States, Phys. Rev. Lett. **101**, 120403 (2008).

[23] A. R. Akhmerov, J. Nilsson, and C. W. J. Beenakker, Electrically Detected Interferometry of Majorana Fermions in a Topological Insulator, Phys. Rev. Lett. **102**, 216404 (2009).

[24] L. Fu and C. L. Kane, Probing Neutral Majorana Fermion Edge Modes with Charge Transport, Phys. Rev. Lett. **102**, 216403 (2009).

[25] K. Zhang and Q. Cheng, Electrically tunable crossed Andreev reflection in a ferromagnet–superconductor–ferromagnet junction on a topological insulator, Supercond. Sci. Technol. **31**, 075001 (2018).

[26] F. Keidel, S.-Y. Hwang, B. Trauzettel, B. Sothmann, and P. Burset, On-demand thermoelectric generation of equal-spin Cooper pairs, Phys. Rev. Research **2**, 022019(R) (2020).

[27] G. Blasi, F. Taddei, V. Giovannetti, and A. Braggio, Manipulation of cooper pair entanglement in hybrid topological Josephson junctions, Phys. Rev. B **99**, 064514 (2019).

[28] W. Chen, R. Shen, L. Sheng, B. G. Wang, and D. Y. Xing, Resonant nonlocal Andreev reflection in a narrow quantum spin Hall system, Phys. Rev. B **84**, 115420 (2011).

[29] R. W. Reinthaler, P. Recher, and E. M. Hankiewicz, Proposal for an All-Electrical Detection of Crossed Andreev Reflection in Topological Insulators, Phys. Rev. Lett. **110**, 226802 (2013).

[30] F. Crépin, P. Burset, and B. Trauzettel, Odd-frequency triplet superconductivity at the helical edge of a topological insulator, Phys. Rev. B **92**, 100507(R) (2015).

[31] C. Fleckenstein, N. T. Ziani, and B. Trauzettel, Conductance signatures of odd-frequency superconductivity in quantum spin Hall systems using a quantum point contact, Phys. Rev. B **97**, 134523 (2018).

[32] J. Cayssol, Crossed Andreev Reflection in a Graphene Bipolar Transistor, Phys. Rev. Lett. **100**, 147001 (2008).

[33] D. Breunig, P. Burset, and B. Trauzettel, Creation of Spin-Triplet Cooper Pairs in the Absence of Magnetic Ordering, Phys. Rev. Lett. **120**, 037701 (2018).

[34] SK Firoz Islam, P. Dutta, and A. Saha, Enhancement of crossed Andreev reflection in a normal-superconductor-normal junction made of thin topological insulator, Phys. Rev. B **96**, 155429 (2017).

[35] F. de Juan, R. Ilan, and J. H. Bardarson, Robust Transport Signatures of Topological Superconductivity in Topological Insulator Nanowires, Phys. Rev. Lett. **113**, 107003 (2014).

[36] Y. Zhang and A. Vishwanath, Anomalous Aharonov-Bohm Conductance Oscillations from Topological Insulator Surface States, Phys. Rev. Lett. **105**, 206601 (2010).

[37] P. M. Ostrovsky, I. V. Gornyi, and A. D. Mirlin, Interaction-Induced Criticality in $\mathbb{Z}_2$ Topological Insulators, Phys. Rev. Lett. **105**, 036803 (2010).

[38] A. Cook and M. Franz, Majorana fermions in a topological-insulator nanowire proximity-coupled to an *s*-wave superconductor, Phys. Rev. B **84**, 201105(R) (2011).

[39] A. M. Cook, M. M. Vazifeh, and M. Franz, Stability of Majorana fermions in proximity-coupled topological insulator nanowires, Phys. Rev. B **86**, 155431 (2012).

[40] D.-H. Lee, Surface States of Topological Insulators: The Dirac Fermion in Curved Two-Dimensional Spaces, Phys. Rev. Lett. **103**, 196804 (2009).

[41] O. Vafek, Quantum Hall effect in a singly and doubly connected three-dimensional topological insulator, Phys. Rev. B **84**, 245417 (2011).

[42] Y.-Y. Zhang, X.-R. Wang, and X. C. Xie, Three-dimensional topological insulator in a magnetic field: Chiral side surface

states and quantized Hall conductance, J. Phys.: Condens. Matter **24**, 015004 (2011).

[43] L. Brey and H. A. Fertig, Electronic states of wires and slabs of topological insulators: Quantum Hall effects and edge transport, Phys. Rev. B **89**, 085305 (2014).

[44] J. Ziegler, R. Kozlovsky, C. Gorini, M.-H. Liu, S. Weishäupl, H. Maier, R. Fischer, D. A. Kozlov, Z. D. Kvon, N. Mikhailov, S. A. Dvoretsky, K. Richter, and D. Weiss, Probing spin helical surface states in topological HgTe nanowires, Phys. Rev. B **97**, 035157 (2018).

[45] This is the special case of [43] for $A_1 = A_2 = \hbar v_F$ and $D_1 = D_2 = 0$.

[46] H. Zhang, C.-X. Liu, X.-L. Qi, X. Dai, Z. Fang, and S.-C. Zhang, Topological insulators in $Bi_2Se_3$, $Bi_2Te_3$ and $Sb_2Te_3$ with a single Dirac cone on the surface, Nat. Phys. **5**, 438 (2009).

[47] L. Susskind, Lattice fermions, Phys. Rev. D **16**, 3031 (1977).

[48] H. Nielsen and M. Ninomiya, A no-go theorem for regularizing chiral fermions, Phys. Lett. B **105**, 219 (1981).

[49] R. Stacey, Eliminating lattice fermion doubling, Phys. Rev. D **26**, 468 (1982).

[50] R. Peierls, Zur Theorie des Diamagnetismus von Leitungselektronen, Z. Phys. **80**, 763 (1933).

[51] C. W. Groth, M. Wimmer, A. R. Akhmerov, and X. Waintal, Kwant: A software package for quantum transport, New J. Phys. **16**, 063065 (2014).

[52] P. R. Amestoy, I. S. Duff, J.-Y. L'Excellent, and J. Koster, A fully asynchronous multifrontal solver using distributed dynamic scheduling, SIAM J. Matrix Anal. Appl. **23**, 15 (2001).

[53] P. R. Amestoy, A. Buttari, J.-Y. L'Excellent, and T. Mary, Performance and scalability of the block low-rank multifrontal factorization on multicore architectures, ACM Trans. Math. Softw. **45**, 1 (2019).

[54] C. J. Lambert and R. Raimondi, Phase-coherent transport in hybrid superconducting nanostructures, J. Phys.: Condens. Matter **10**, 901 (1998).

[55] C.-X. Liu, X.-L. Qi, H. J. Zhang, X. Dai, Z. Fang, and S.-C. Zhang, Model Hamiltonian for topological insulators, Phys. Rev. B **82**, 045122 (2010).

[56] K. Moors, P. Schüffelgen, D. Rosenbach, T. Schmitt, T. Schäpers, and T. L. Schmidt, Magnetotransport signatures of three-dimensional topological insulator nanostructures, Phys. Rev. B **97**, 245429 (2018).

[57] G. W. Winkler, A. E. Antipov, B. van Heck, A. A. Soluyanov, L. I. Glazman, M. Wimmer, and R. M. Lutchyn, Unified numerical approach to topological semiconductor-superconductor heterostructures, Phys. Rev. B **99**, 245408 (2019).

[58] F. de Juan, J. H. Bardarson, and R. Ilan, Conditions for fully gapped topological superconductivity in topological insulator nanowires, Sci. Post Phys. **6**, 60 (2019).

[59] D. Rosenbach, N. Oellers, A. R. Jalil, M. Mikulics, J. Kölzer, E. Zimmermann, G. Mussler, S. Bunte, D. Grützmacher, H. Lüth, and T. Schäpers, Quantum transport in topological surface states of selectively grown $Bi_2Te_3$ nanoribbons, Adv. Electron. Mater. **6**, 2000205 (2020).

[60] White-noise disorder is a stronger scattering source than disorder with longer-range correlations. It is good for the "stress test" of CAR and also appropriate for the relatively small size of our test system.

[61] Y. Chen, H.-Z. Lu, and X. C. Xie, Forbidden Backscattering and Resistance Dip in the Quantum Limit as a Signature for Topological Insulators, Phys. Rev. Lett. **121**, 036602 (2018).

[62] A. Wolos, S. Szyszko, A. Drabinska, M. Kaminska, S. G. Strzelecka, A. Hruban, A. Materna, M. Piersa, J. Borysiuk, K. Sobczak, and M. Konczykowski, *g*-factors of conduction electrons and holes in $Bi_2Se_3$ three-dimensional topological insulator, Phys. Rev. B **93**, 155114 (2016).